metals

MDPI

Article

Machine Learning-Based Prediction of High Cycle Fatigue and Fatigue Crack Growth Rate in LPBF Co-Cr-Mo Alloys Under Varying Scanning Strategies

Vinod Kumar Jat [1], Roshan Udaram Patil [1], Manish Kumar [2] and Denis Benasciutti [2,*]

[1] Mechanical Engineering Department, Indian Institute of Technology Jammu, Jammu 181221, India; vinod.jat@iitjammu.ac.in (V.K.J.); roshan.patil@iitjammu.ac.in (R.U.P.)
[2] Polytechnic Department of Engineering and Architecture (DPIA), University of Udine, Via delle Scienze 206, 33100 Udine, Italy; manish.kumar@uniud.it
* Correspondence: denis.benasciutti@uniud.it

Abstract

This study explores the use of machine learning to predict high-cycle fatigue (HCF) behavior and fatigue crack growth rate (FCGR) in Co-Cr-Mo alloys manufactured through laser powder bed fusion. Two machine learning (ML) models: extreme gradient boosting (XGB) and deep neural networks (DNN), are implemented to estimate HCF and FCGR across three distinct scanning strategies. The raw datasets for HCF and FCGR are taken from previously performed experiments. The HCF dataset is augmented using a Gaussian Mixture Model, while the FCGR dataset is used in its raw form. Following hyperparameter optimization, both models exhibited quite similar accuracy on validation datasets. Their performance is assessed during testing using mean squared error (MSE) and R^2 scores. The DNN model demonstrated higher accuracy in HCF predictions by achieving higher R^2 scores. The DNN performs better because it can handle more complex patterns effectively due to its multiple neurons and deeper multilayer architecture. In contrast, the XGB model performed better in FCGR predictions and yielded higher R^2 scores compared to XGB. The good agreement with the experimental dataset shows that these two ML techniques are effective in predicting HCF and FCGR behavior.

Keywords: machine learning; XGB; DNN; scanning strategy; Co-Cr-Mo alloy; fatigue

1. Introduction

Mostly, the key components of bio-implants [1,2] and aerospace structures [3] have intricated shapes that undergo complex repeated loadings. These loadings result in fatigue damage, which combines with environmental factors and leads to premature failures. Therefore, a complete fatigue understanding is an important aspect in the material design process. Recently, additively fabricated Co-Cr-Mo alloy has garnered notable attention across several sectors due to its exceptional combination of mechanical properties [2], corrosion resistance [3], biocompatibility [4], wear resistance [5] and admirable strength-to-weight ratio for lightweight lattice structures [6]. The fatigue behavior of additively fabricated components/parts depends on various process parameters, including build orientation [7,8], layer thickness, scanning strategy [9], scanning speed [10], and many more.

Conventional methods of fatigue assessment depend on extensive, time-consuming, and costly experiments, yet their ability to generalize is limited by the experimental ranges.

Academic Editor: Dariusz Rozumek

Received: 24 December 2025
Revised: 9 February 2026
Accepted: 22 February 2026
Published: 25 February 2026

https://doi.org/10.3390/met16030249

To overcome this limitation, numerous numerical predictive methods (such as S-N curve-based models, Paris law model, probabilistic fatigue approaches, and machine learning based techniques) have emerged that eliminate the need for these labor-intensive experiments. Among these methods, machine learning (ML) is a viable solution [11,12]. ML is recognized by the scientific community very quickly due to its ability to analyze complex relationships between variables and make predictions. Various regression models can be incorporated into ML, such as XGBoost (XGB) [13], Support Vector Regression (SVR) [14], k-nearest neighbor algorithm (KNN) [15] and Deep Neural Networks (DNN) [16]. These methods have specific advantages: XGB utilizes greedy algorithms and parallel processing to enhance training and prediction speeds [17], SVR exhibits strong generalization ability on small datasets and excellent robustness to overfitting [18], KNN is particularly useful when there is little or no prior knowledge about the distribution of the data [19], and DNN are feasible for application to both small dataset [20] as well as large dataset [21]. ML is a powerful tool for modeling vast amounts of data without relying on physical mechanisms. ML-based data mining techniques have been widely applied in fatigue analysis to uncover potential relationships between test parameters and material fatigue properties using large datasets.

In the past, several ML techniques have been explored to predict fatigue life using various algorithms. For instance, Li et al. [11] applied an artificial neural network (ANN) model to predict the fatigue life of laser powder bed fusion (LPBF) printed Ti-6Al-4V using stress, build orientation, defect size, defect depth, and defect distance to the surface as input parameters. A single hidden layer with the Levenberg–Marquardt algorithm, along with a feedforward backpropagation ANN model, was implemented and achieved a good correlation between actual and predicted fatigue life, with an R^2 value of 0.98. Braun and Kellner [22] used gradient-boosted tree machine learning models to analyze fatigue behavior and employed the SHapley Additive explanation (SHAP) framework to examine the significance of features and their interactions in relation to the predictions. Zhan and Li [23] compared three ML models (RF, SVM, and ANN) for predicting the fatigue life of additively fabricated SS316L in relation to continuum damage mechanics. Parametric study of these models found that RF achieved the highest R^2 value, while support vector machine (SVM) resulted in the highest mean square error (MSE). Shi et al. [24] used various methods for data augmentation (linear interpolation, nearest neighbor interpolation, and linear interpolation with a Gaussian mixture model) for very high-cycle fatigue data (stress amplitude, fatigue life, defect size, defect location, and defect circularity) of LPBF fabricated AlSi10Mg to predict fatigue life using various ML models (ANN, RF, and support vector regression). It was observed that linear interpolation with a Gaussian mixture model generated a virtual dataset that was similar to the original dataset, and the RF model performed the best in predicting fatigue life among the other models. Bao et al. [14] compared support vector regression (SVR) and k-nearest neighbor algorithm (KNN) methods for fatigue life prediction of LPBF fabricated Ti-6Al-4V that led to the development of a relationship between fatigue life and synchrotron X-ray tomography (defect size, location, and morphology) using ML models. These findings showed that the SVR model achieved a higher R^2 value and lower MSE for the predicted fatigue life. Konda et al. [25] demonstrated that the XGB method achieved a higher R^2 value and lower MSE for predicting the fatigue crack growth behavior of LPBF-fabricated 17-4PH.

To date, few studies have addressed fatigue life prediction and fatigue crack growth behavior using machine-learning techniques in relation to process parameters. However, no reported work has applied XGB and DNN models to predict fatigue life and fatigue crack growth rate in LPBF-fabricated Co-Cr-Mo alloys.

This study applies XGB and DNN models to predict HCF life and FCGR of LPBF-fabricated Co-Cr-Mo alloy using the leave-one-group-out technique. Experimental fatigue data for three scanning strategies (stripe (S), meander (M), and chessboard (CH)) are obtained from previous studies performed by the authors. The HCF dataset consists of 21 data points and is augmented using a Gaussian mixture model (GMM), while the FCGR dataset is used without post-processing. The XGB and DNN models are trained to predict HCF life and FCGR for different scanning strategies. Model predictions are validated against previously reported experimental results, followed by a comparative performance analysis of the XGB and DNN models.

2. Material and Methods

This section presents the materials, testing procedures, and post-processing of the raw data obtained from both the HCF and FCGR experiments.

2.1. Material and Tests

In this investigation, Co-Cr-Mo alloy powder manufactured through gas atomization by Renishaw® (Wotton-under-Edge, UK) was utilized. The material composition, containing approximately 27–30 wt.% Cr and 5–7 wt.% Mo, with trace amounts (<1 wt.%) of Mn and Si, less than 0.75 wt.% Fe, under 0.50 wt.% Ni, and the remainder is composed of cobalt. Additive manufacturing was carried out via Laser Powder Bed Fusion (LPBF) on a Renishaw® AM400 system. The processing parameters used for the additive manufacturing in this study are shown in Table 1. Specimens were printed with three scanning strategies, i.e., stripe (S), meander (M), and chessboard (CH). Under the stripe scanning approach, the stripe width was fixed at 5 mm. In the meander scanning approach, the laser scanned the complete layer using one uninterrupted trajectory. The chessboard scanning approach divided the layer into multiple islands, each with dimensions of 5 × 5 mm^2.

Table 1. The process parameters used to print the specimens.

Power (W)	Hatch Spacing (µm)	Laser Spot Diameter (µm)	Layer Thickness (µm)
200	100	70	30

In previous studies, two types of experiments: high-cycle fatigue (HCF) and fatigue crack growth rate (FCGR) tests were conducted. These experimental datasets were used for model training and prediction processes. The HCF tests were performed at a frequency of 15 Hz with a load ratio of 0.1 across seven different maximum stress levels. The FCGR tests were carried out at a frequency of 10 Hz with a load ratio of 0.1 and included both pre-cracking and main crack growth stages. The pre-cracking stage employed the decreasing stress intensity factor (K-decreasing) method, while the main crack growth tests were conducted under constant load conditions. However, the details of material, printing setting and all experimental results are given in pervious study [26,27].

2.2. Experimental Data

The maximum stress and number of cycles, along with the generated S-N curves, are taken from the previous study by the authors [26]. The actual experimental data of the HCF test for all three scanning strategies are shown in Figure 5a. This sparse data (21 data points) of the HCF test makes it challenging to generalize an ML predictive model, as models trained on small datasets often encounter overfitting. The scatter or variability of features further increases the likelihood of overfitting in models trained on small datasets, leading to poor generalization. To address these challenges, the dataset is augmented using

GMM. GMM is a probabilistic model that assumes data points are derived from a mixture of a limited number of Gaussian distributions [28,29]. The probability distribution of GMM can be written as

$$P(x \mid \theta) = \sum_{j=1}^{J} \sum_{k=1}^{K} \alpha_k \phi(x_j \mid \theta_k) \tag{1}$$

where x_j is j-th observed data, J denotes the number of data points, K represents the number of Gaussian models in mixture model, α_k represents probability that the observation belongs to k-th sub model, and θ_k is the corresponding parameters. A total of 21 data points (7 for each scanning strategy) are expanded to 600 data points corresponding to three different scanning strategies. The augmented data points are constrained within a stress range of 350 MPa to 130 MPa or until the number of cycles reached one million at the corresponding maximum stress. For the fatigue crack growth dataset, the original raw data comprising 446 data points is adopted from the previous study [27]. This dataset includes combined data from all three scanning strategies and covers both the near-threshold and Paris regions of crack growth behavior. The actual experimental data of the FCGR test for all three scanning strategies are shown in Figure 8a. As the dataset size is comparable to that of the HCF dataset, data augmentation is not employed.

Before selecting an ML model, it is crucial to transform the experimental data. For the application of the HCF and FCGR prediction models, the training process is expected to be highly time-consuming. To mitigate this, data normalization is applied in this work, scaling the data within the range of zero to unity.

3. ML Models

The details of ML procedure for both the XGB and DNN models are also described in this section.

3.1. Extreme Gradient Boosting

Extreme gradient boosting is an advanced boosting ensemble technique designed to enhance both predictive accuracy and computational efficiency. It integrates L1 and L2 regularization to reduce overfitting and improve generalization. Using decision trees as base learners, each tree is trained to correct the errors of its predecessors. The algorithm optimizes the training process and model performance by prioritizing speed and accuracy. Additionally, XGB applies gradient descent optimization to minimize the loss function to ensure a closer match between predicted and actual values. Figure 1 depicts the decision-making process, including the root node, intermediate nodes, and leaf nodes. The objective formula combines the loss function with a regularization term as follows [30],

$$obj(\theta) = \sum_{i=1}^{n} l(\hat{y}, y_i) + \sum_{k=1}^{K} \Omega(f_k) \tag{2}$$

where l is loss function and $\Omega(f_k)$ is the regularization term which penalizes the complexity of the tree as

$$\Omega(f_k) = \gamma\, K + 0.5\, \lambda \sum_{j=1}^{K} w_j^2 \tag{3}$$

where γ is a parameter that controls the minimum loss reduction required to make a further partition of number of trees in XGB, K is the number of leaves in the tree, and λ is the regularization term on the weights w_j. The leave-one-group-out technique is applied, where the S and CH scanning strategies are used for training and validation, while the M scanning strategy is used for testing. The processed experimental dataset is divided into training and validation sets, with 80% allocated for training and 20% for validation from each strategy. The HCF training dataset contained 384 data points, while the FCGR training dataset comprised 286 data points.

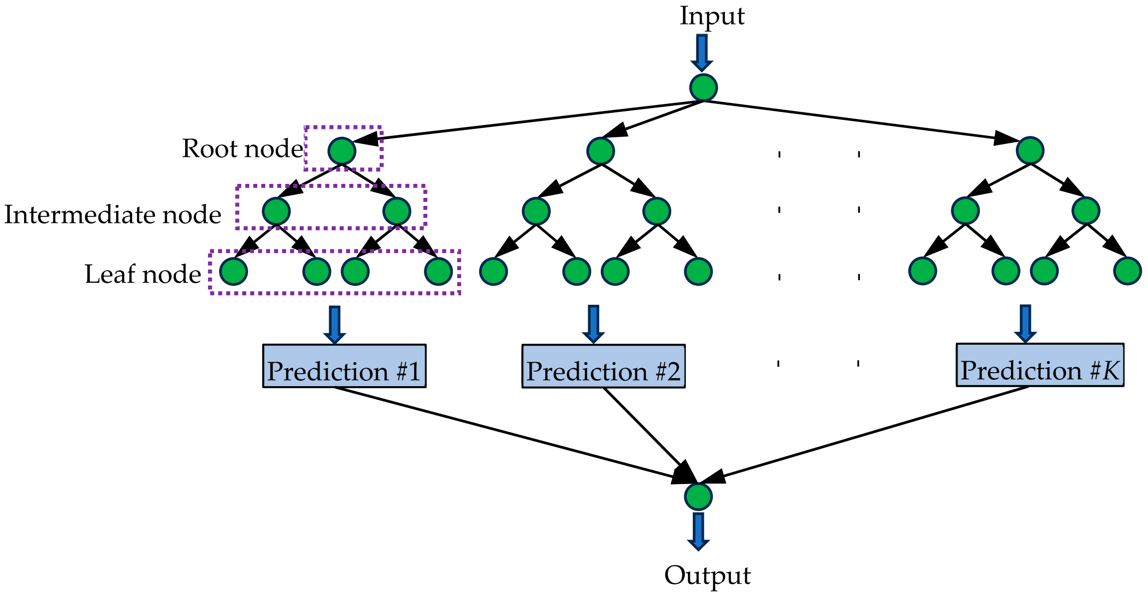

Figure 1. The schematic illustration of the XGB decision tree model architecture.

Two commonly used metrics for assessing the precision and performance of a machine learning model are the R^2 (coefficient of determination) and MSE, as shown in Equations (4) and (5).

$$R^2 = 1 - \frac{\sum_{i=1}^{n} \left(P_i - P_i^{pre}\right)^2}{\sum_{i=1}^{n} \left(P_i - P_{mean}\right)^2} \tag{4}$$

$$\text{MSE} = \frac{1}{n} \sum_{i=1}^{n} \left(P_i - P_i^{pre}\right)^2 \tag{5}$$

where P_i represents the i-th value in the dataset, P_i^{pre} is the i-th predicted value, and P_{mean} denotes the mean of the dataset. A higher R^2 indicating a better model fit, where R^2 value ranges from 0 to 1. MSE measures the average difference between the dataset and the predicted results, where a smaller MSE indicates more accurate predictions. MSE is calculated on the normalized dataset.

The optimized hyperparameters are determined through sensitivity analysis of two parameters: maximum depth (ranging from 2 to 10) and the number of estimators (100, 200, 400, 500, and 1000). MSE is computed for these values of the parameters and later compared to finding out the optimized hyperparameters. This comparison is illustrated in Figure 2, and the hyperparameters corresponding to the minimum loss values are selected as the optimized hyperparameters. Table 2 presents the optimized hyperparameters for the XGB method for both tests.

Table 2. The optimized hyperparameters used in this study for the XGB method.

Hyperparameters	**Booster**	**Learning Rate**	**Regularization Term (λ)**	**Maximum Depth**	**Number of Estimators**	**Min. Child Weight**	**Random State**
HCF	GB tree	0.1	0.5	5	500	2	30
FCGR				7	1000		42

https://doi.org/10.3390/met16030249

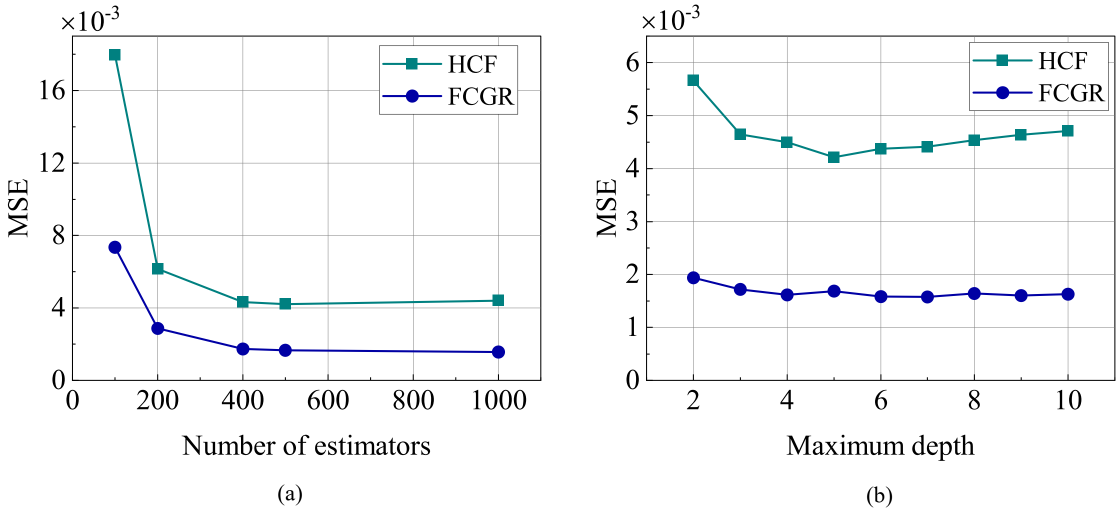

Figure 2. The hyperparameter sensitivity analysis of the XGB model for both tests for (**a**) number of estimators and (**b**) maximum depth.

3.2. Deep Neural Network

Deep Neural Network (DNN) is an ML model designed to capture complex input–output relationships. As a part of supervised learning, DNNs consist of multiple hidden layers, making them highly powerful for pattern recognition. These networks consist of an input layer, hidden layers, and an output layer [31]. The training process includes both forward and backward passes, where the loss function is optimized using techniques like Gradient Descent and Adaptive Moment Estimation (Adam) [32]. Figure 3 illustrates the full schematic representation of the input, hidden, and output layers.

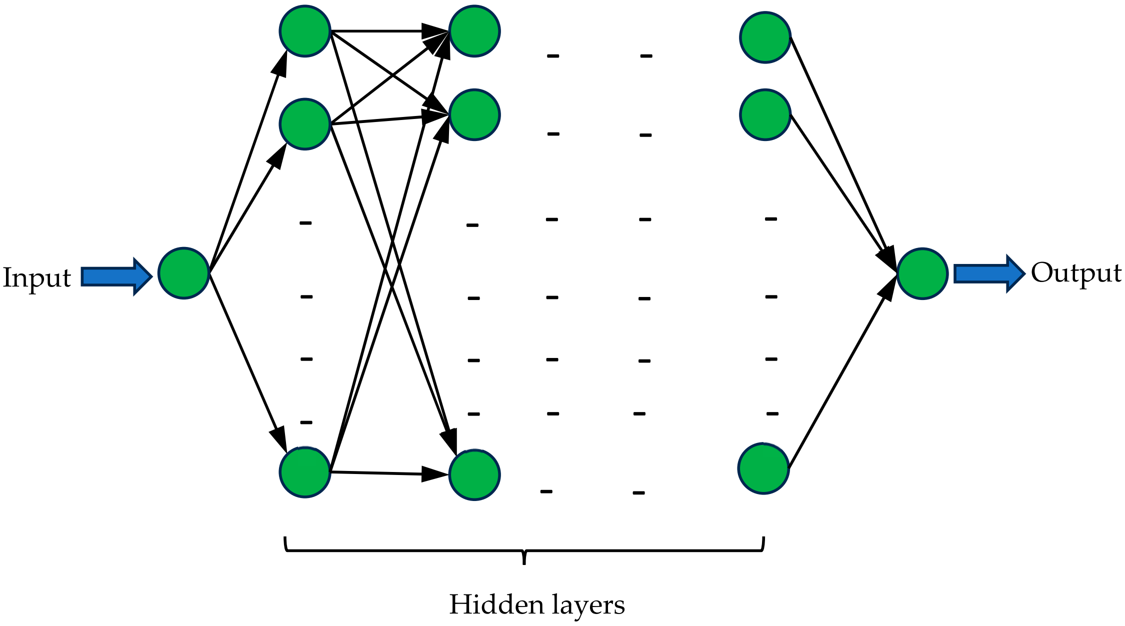

Figure 3. The schematic illustrations of the DNN model architecture.

A typical forward propagation learning process used in the DNN model is given by Equation (6),

$$\hat{y}_k^n(w,b) = \mathrm{A}(x) =: \mathrm{A}\left(\sum_{i=1}^{m} w_i^{n-1} \cdot \hat{y}_i^{n-1} + b_k^{n-1}\right) \tag{6}$$

where the forward propagation output of k-th neuron for nth layer is $\hat{y}_k^n$, w_i^{n-1} is weight of i-th neuron for $(n-1)$-th layer, $\hat{y}_i^{n-1}$ is the output of i-th neuron for $(n-1)$-th layer,

b_k^{n-1} is the bias of k-th neuron for $(n-1)$-th layer and A(x) is the activation function. For this study, the exponential linear unit (ELU) is used as an activation function that can be expressed as [33],

$$\mathrm{A}(x) = \begin{cases} x, & \text{if } x > 0 \\ \alpha(e^x - 1), & \text{if } x \le 0 \end{cases} \tag{7}$$

where x is the input to the neuron, α is a constant, and its value is 1. The loss (L) of each layer is calculated in terms of MSE as expressed in Equation (8) as

$$L(y_i, \hat{y}_i) = \frac{1}{n}\sum_{i=1}^{n} (\hat{y}_i - y_i)^2 \tag{8}$$

where $\hat{y}$ is the model's predictions and y_i is the actual target values.

Following forward propagation, the loss function is minimized through backpropagation, as described in Equation (8), with the help of Adam optimizer. In this method, the data is also divided in the same manner as used for XGB. The hyperparameters are derived from a sensitivity analysis of two factors: the number of hidden layers (ranging from 5 to 30 in increments of 5) and the neurons on each layer (16, 24 and 32). These factors are used to evaluate MSE. The evaluated MSE is compared to find the optimized hyperparameters. This comparison is presented in Figure 4, and the hyperparameters corresponding to the minimum loss values are selected as the optimized hyperparameters. Table 3 outlines the optimized hyperparameters for the DNN method in both experiments.

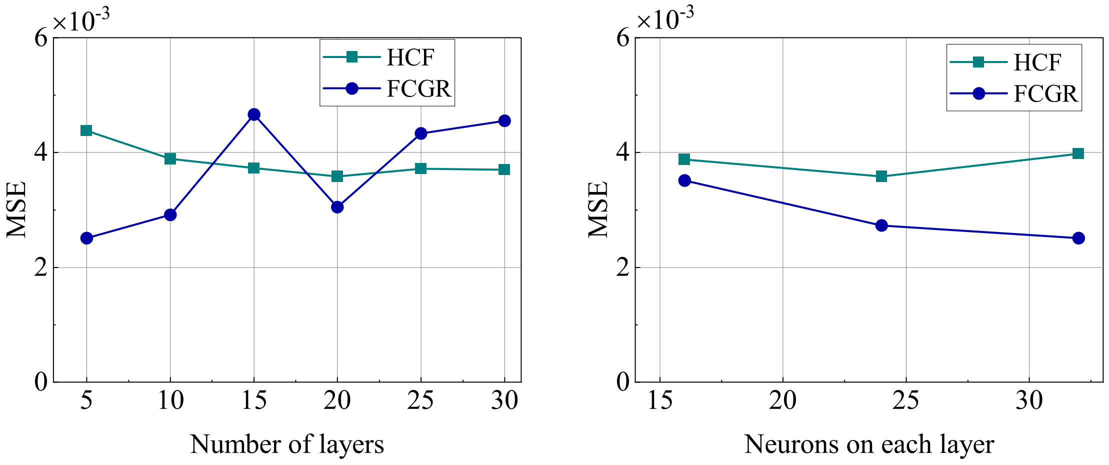

(a)

(b)

Figure 4. The hyperparameter sensitivity analysis of the DNN model for both tests for (**a**) number of layers and (**b**) neurons on each layer.

Table 3. The optimized hyperparameters used in this study for DNN method.

Hyperparameters	Number of Hidden Layers	Learning Rate (Adam)	Neurons on Each Layer	Batch Size	Drop Out	Epochs	Random Seed
HCF	20	0.01	24	27	0.02	200	42
FCGR	5		32	15			30

4. Results and Discussion

In this section, the predicted results from both the XGB and DNN models are presented and compared with the experimental results from the previous studies [26,27]. A detailed discussion is provided on various aspects of the predictions for all scanning strategies.

4.1. High Cycle Fatigue

The maximum stress vs. number of cycles curve is a physical–statistical model. It applies empirical formulas (such as Basquin's equation) to determine parameters that describe the degradation of material strength under fatigue loading. However, ML uses fatigue data to train models and map a nonlinear relationship between the AM process parameters, operating conditions, and fatigue life [34,35].

The maximum stress and scanning strategies (S and CH) are considered as input parameters for both models. The leave-one-group-out is applied, so the M strategy is kept for the test. The output layer contains a single output: fatigue life for the M strategy. The optimized hyperparameters for both models are listed in the previous section. The predicted and actual experimental fatigue life for all the conditions is compared for both models, as shown in Figure 5. The arrows in Figure 5 denote the run-out specimens (more than 1 × 10^6 cycles). A comparison of the predicted results from models trained on the original experimental dataset indicates that the models perform accurately. For the test dataset, the R^2 and MSE are 0.82 and 1.3×10^{-2} for XGB, and 0.87 and 3.7×10^{-3} for DNN, respectively, as shown in Table 4. Both the XGB and DNN models show almost identical prediction accuracy, as shown in Table 4. However, the DNN provides better accuracy and a lower MSE compared to XGB. Figure 6a,b illustrates the relationship between the loss (i.e., normalized mean squared error) and boosting rounds for the XGB model and the epochs for the DNN model. The plot shows that the loss rapidly converges to a global minimum, indicating that the XGB and DNN models are well-suited to the data and are able to optimize efficiently in a short time. The loss curves are presented for both the training and validation datasets. The predicted data showed good accuracy compared to the actual data, as shown in Figure 7 (all data fell within 3 error band).

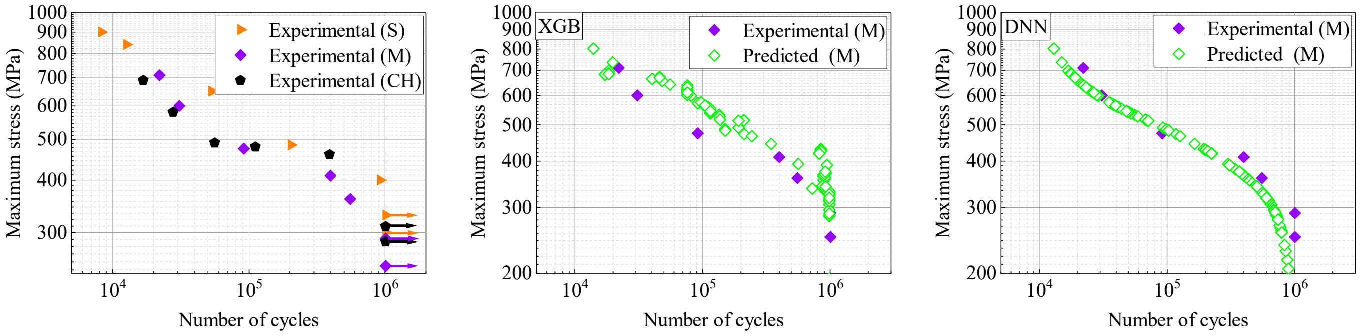

(a) (b) (c)

Figure 5. (**a**) actual experimental plot (reprinted with permission from ref. [26]. 2024 Springer Nature) of the maximum stress vs. number of cycles. The comparison of predicted data for scanning strategies M of LPBF printed Co-Cr-Mo alloy with (**b**) XGB and (**c**) DNN model.

Table 4. The evaluation metrics for the HCF test predicted test data set for both models.

Model	R^2	MSE
XGB	0.82	1.3×10^{-2}
DNN	0.87	3.7×10^{-3}

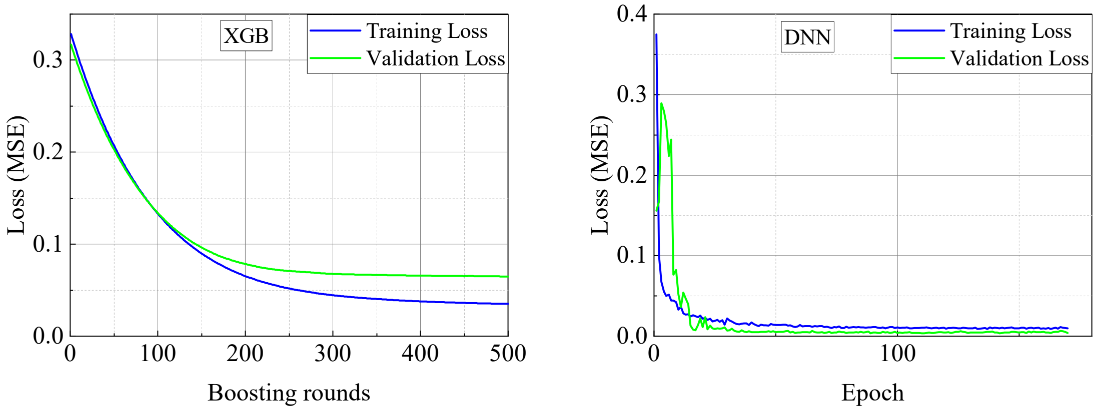

(a) (b)

Figure 6. The loss performance of the (**a**) XGB and (**b**) DNN model for the HCF data set.

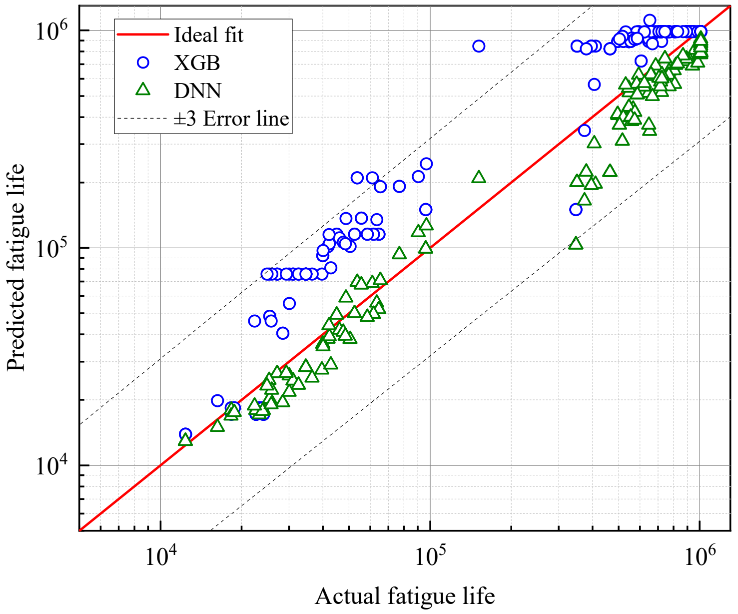

Figure 7. Predicted fatigue life vs. experimental fatigue life (reprinted with permission from ref. [26]. 2024 Springer Nature) plot for HCF test data set of both XGB and DNN models.

4.2. Fatigue Crack Growth

The input parameters for both models include crack length (a), number of cycles (N), stress intensity factor range (ΔK), and scanning strategies (S and CH). The output layer produces a single result: crack growth rate ($\mathrm{d}a/\mathrm{d}N$) of the M strategy as per leave-one-group-out. The predicted data set and actual experimental data are compared for both models, as shown in Figure 8. This comparison is not limited to the Paris region; it also reveals the threshold region, which distinguishes it from linear regression. The predicted results showed a high degree of accuracy when compared to the actual data, as seen in Figure 8. The prediction results from models trained on the original experimental dataset for FCGR indicate that both models perform accurately. For the test dataset, the R^2 and MSE are 0.84 and 2.7×10^{-3} for XGB, and 0.77 and 4×10^{-3} for DNN, respectively, as shown in Table 5. Among these, the XGB model delivers the higher prediction accuracy, as shown in Table 5. Figure 9 illustrates the relationship between loss (normalized mean squared error) and boosting rounds for the XGB model, and between loss (normalized mean squared error) and epochs for the DNN model. The plot clearly shows that the loss rapidly converges to a global minimum, enabling the model to optimize efficiently in a short period. The predicted data showed good accuracy compared to the actual data, as shown in Figure 10 (all data fell within 3 error band).

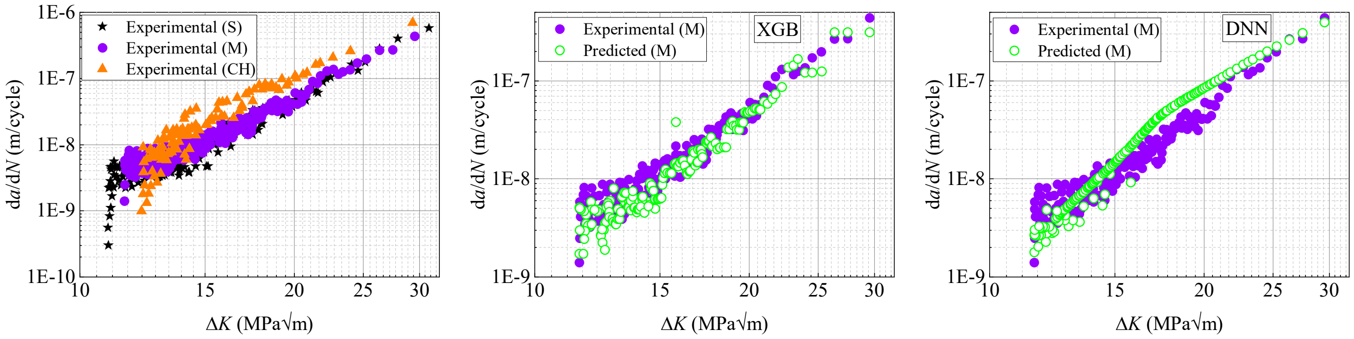

(a) (b) (c)

Figure 8. (**a**) Actual experimental plot (reprinted with permission from ref. [27]. 2024 Elsevier) of the stress intensity factor range vs. crack growth rate. The comparison of the predicted data for scanning strategies M of LPBF printed Co-Cr-Mo alloy, based on (**b**) the XGB and (**c**) the DNN model.

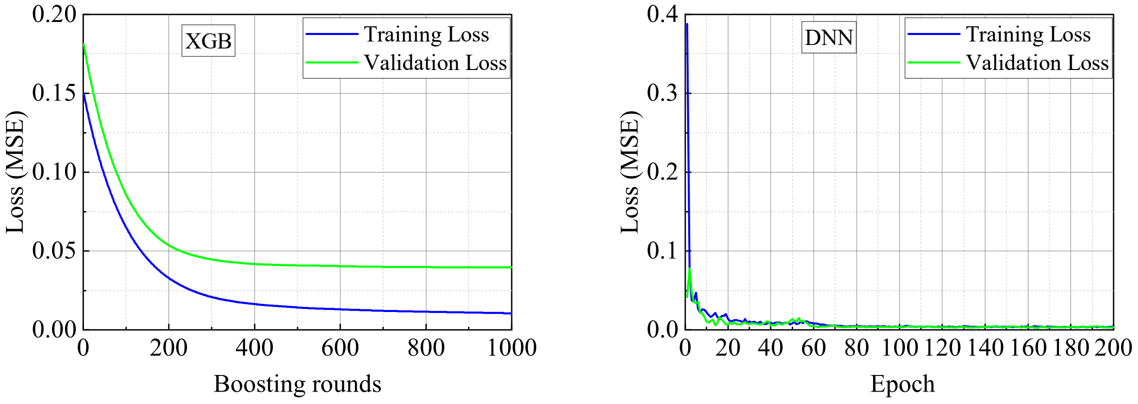

(a) (b)

Figure 9. The loss performance of the (**a**) XGB and (**b**) DNN model for the FCGR data set.

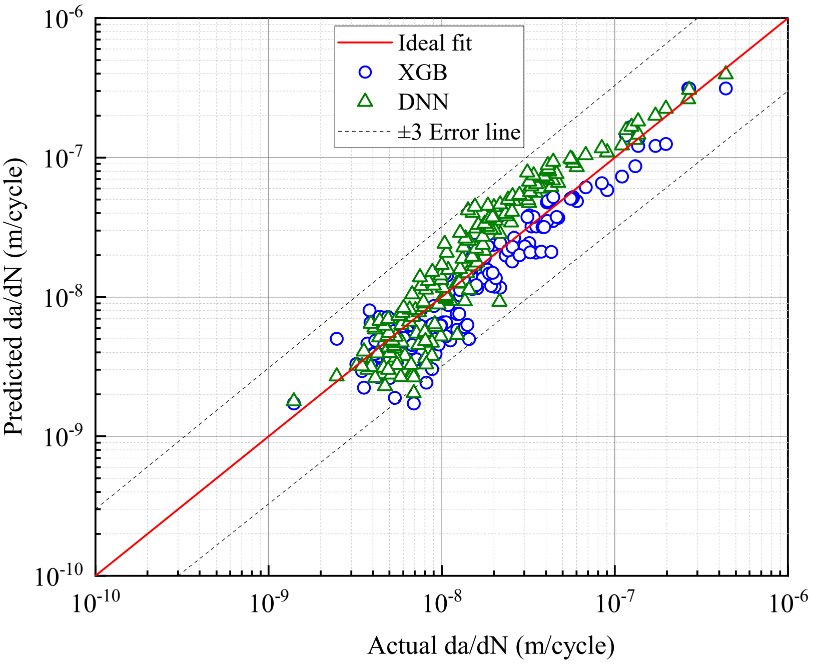

Figure 10. Predicted fatigue life vs. actual fatigue life (reprinted with permission from ref. [27]). 2024 Elsevier) plot for HCF test data set of both XGB and DNN models.

Table 5. The evaluation metrics for the FCGR test predicted test data set for both models.

Model	R^2	MSE
XGB	0.84	2.7×10^{-3}
DNN	0.77	4×10^{-3}

5. Conclusions

In this study, XGB and DNN machine learning models are used to predict fatigue life and crack growth rate for high-cycle fatigue and fatigue crack growth tests under three different scanning strategies. The key conclusions derived from the observed results and discussions are as follows:

1. Both ML models demonstrated similar accuracy and performance on the test data for all three scanning strategies.
2. The HCF test data are more sensitive to hyperparameters as compared to the FCGR data set.
3. For the HCF test dataset, both models showed comparable performance in terms of R^2; however, the DNN model achieved marginally higher accuracy owing to its deeper multilayer architecture and greater capacity to capture complex patterns. Conversely, for the FCGR test dataset, the XGB model outperformed the DNN and achieved a higher R^2.
4. Both models (XGB and DNN) showed predicted life for the HCF test dataset and fatigue crack growth rate for FCGR are within three error bands.

Based on machine learning models such as XGBoost and deep neural networks, two scanning strategies are used for training to predict the third scanning strategy, thereby reducing the experimental cost associated with the third strategy.

Author Contributions: Conceptualization, V.K.J.; Methodology, V.K.J.; Validation, V.K.J. and R.U.P.; Formal analysis, V.K.J.; Investigation, V.K.J., R.U.P., M.K. and D.B.; Resources, R.U.P. Writing—original draft, V.K.J.; Writing—review and editing, V.K.J., R.U.P., M.K. and D.B.; Visualization, V.K.J.; Supervision, M.K. and R.U.P.; Project administration, M.K. and D.B.; Funding acquisition, M.K. All authors have read and agreed to the published version of the manuscript.

Funding: This research is funded by Programma Operativo Complementare (POC) 2014–2020 della Regione Autonoma Friuli Venezia Giulia—CUP G23C25000880002—CODICE OPERAZIONE 2025/13846—CODICE PROGETTO 2025/13846/6.

Data Availability Statement: The original contributions presented in this study are included in the article. Further inquiries can be directed to the corresponding author.

Acknowledgments: The authors would like to express their sincere gratitude for the funding and support received from the Ministry of Education (MoE), Government of India.

Conflicts of Interest: The authors declare no conflicts of interest.

References

1. Acharya, S.; Gopal, V.; Gupta, S.K.; Nilawar, S.; Manivasagam, G.; Suwas, S.; Chatterjee, K. Anisotropy of Additively Manufactured Co–28Cr–6Mo Influences Mechanical Properties and Biomedical Performance. *ACS Appl. Mater. Interfaces* **2022**, *14*, 21906–21915. [CrossRef]
2. Yoda, K.; Suyalatu; Takaichi, A.; Nomura, N.; Tsutsumi, Y.; Doi, H.; Kurosu, S.; Chiba, A.; Igarashi, Y.; Hanawa, T. Effects of Chromium and Nitrogen Content on the Microstructures and Mechanical Properties of As-Cast Co–Cr–Mo Alloys for Dental Applications. *Acta Biomater.* **2012**, *8*, 2856–2862. [CrossRef] [PubMed]
3. Jenko, M.; Gorenšek, M.; Godec, M.; Hodnik, M.; Batič, B.Š.; Donik, Č.; Grant, J.T.; Dolinar, D. Surface Chemistry and Microstructure of Metallic Biomaterials for Hip and Knee Endoprostheses. *Appl. Surf. Sci.* **2018**, *427*, 584–593. [CrossRef]

4. Hedberg, Y.S.; Qian, B.; Shen, Z.; Virtanen, S.; Odnevall Wallinder, I. In Vitro Biocompatibility of CoCrMo Dental Alloys Fabricated by Selective Laser Melting. *Dent. Mater.* **2014**, *30*, 525–534. [CrossRef]
5. Koizumi, Y.; Chen, Y.; Li, Y.; Yamanaka, K.; Chiba, A.; Tanaka, S.-I.; Hagiwara, Y. Uneven Damage on Head and Liner Contact Surfaces of a Retrieved Co–Cr-Based Metal-on-Metal Hip Joint Bearing: An Important Reason for the High Failure Rate. *Mater. Sci. Eng. C* **2016**, *62*, 532–543. [CrossRef]
6. Park, S.-Y.; Kim, K.-S.; AlMangour, B.; Grzesiak, D.; Lee, K.-A. Effect of Unit Cell Topology on the Tensile Loading Responses of Additive Manufactured CoCrMo Triply Periodic Minimal Surface Sheet Lattices. *Mater. Des.* **2021**, *206*, 109778. [CrossRef]
7. Morettini, G.; Razavi, N.; Zucca, G. Effects of Build Orientation on Fatigue Behavior of Ti-6Al-4V as-Built Specimens Produced by Direct Metal Laser Sintering. *Procedia Struct. Integr.* **2019**, *24*, 349–359. [CrossRef]
8. Xu, Z.W.; Liu, A.; Wang, X.S. The Influence of Building Direction on the Fatigue Crack Propagation Behavior of Ti6Al4V Alloy Produced by Selective Laser Melting. *Mater. Sci. Eng. A* **2019**, *767*, 138409. [CrossRef]
9. Roirand, H.; Hor, A.; Malard, B.; Saintier, N. Effect of Laser-scan Strategy on Microstructure and Fatigue Properties of 316L Additively Manufactured Stainless Steel. *Fatigue Fract. Eng. Mater. Struct.* **2023**, *46*, 32–48. [CrossRef]
10. Cao, Y.; Moumni, Z.; Zhu, J.; Gu, X.; Zhang, Y.; Zhai, X.; Zhang, W. Effect of Scanning Speed on Fatigue Behavior of 316L Stainless Steel Fabricated by Laser Powder Bed Fusion. *J. Mater. Process. Technol.* **2023**, *319*, 118043. [CrossRef]
11. Li, J.; Yang, Z.; Qian, G.; Berto, F. Machine Learning Based Very-High-Cycle Fatigue Life Prediction of Ti-6Al-4V Alloy Fabricated by Selective Laser Melting. *Int. J. Fatigue* **2022**, *158*, 106764. [CrossRef]
12. Ben Chaabene, W.; Flah, M.; Nehdi, M.L. Machine Learning Prediction of Mechanical Properties of Concrete: Critical Review. *Constr. Build. Mater.* **2020**, *260*, 119889. [CrossRef]
13. Xiao, L.; Wang, G.; Long, W.; Liaw, P.K.; Ren, J. Fatigue Life Prediction of the FCC-Based Multi-Principal Element Alloys via Domain Knowledge-Based Machine Learning. *Eng. Fract. Mech.* **2024**, *296*, 109860. [CrossRef]
14. Bao, H.; Wu, S.; Wu, Z.; Kang, G.; Peng, X.; Withers, P.J. A Machine-Learning Fatigue Life Prediction Approach of Additively Manufactured Metals. *Eng. Fract. Mech.* **2021**, *242*, 107508. [CrossRef]
15. Kamble, R.G.; Raykar, N.R.; Jadhav, D.N. Machine Learning Approach to Predict Fatigue Crack Growth. *Mater. Today Proc.* **2021**, *38*, 2506–2511. [CrossRef]
16. Chen, S.; Bai, Y.; Zhou, X.; Yang, A. A Deep Learning Dataset for Metal Multiaxial Fatigue Life Prediction. *Sci. Data* **2024**, *11*, 1027. [CrossRef]
17. Wang, Q.; Yao, G.; Kong, G.; Wei, L.; Yu, X.; Jianchuan, Z.; Ran, C.; Luo, L. A Data-Driven Model for Predicting Fatigue Performance of High-Strength Steel Wires Based on Optimized XGBOOST. *Eng. Fail. Anal.* **2024**, *164*, 108710. [CrossRef]
18. Liu, M.; Wang, X.; Mi, D.; Liu, Z.; Long, X.; Wen, S.; Jiang, C. A New Fatigue Life Prediction Method for Welded Joints Based on Machine Learning Incorporating Defect Information and Physics of Failure. *Int. J. Fatigue* **2026**, *202*, 109234. [CrossRef]
19. Guo, K.; Yan, H.; Huang, D.; Yan, X. Active Learning-Based KNN-Monte Carlo Simulation on the Probabilistic Fracture Assessment of Cracked Structures. *Int. J. Fatigue* **2022**, *154*, 106533. [CrossRef]
20. Feng, S.; Zhou, H.; Dong, H. Using Deep Neural Network with Small Dataset to Predict Material Defects. *Mater. Des.* **2019**, *162*, 300–310. [CrossRef]
21. Zhang, X.C.; Gong, J.G.; Xuan, F.Z. A Deep Learning Based Life Prediction Method for Components under Creep, Fatigue and Creep-Fatigue Conditions. *Int. J. Fatigue* **2021**, *148*, 106236. [CrossRef]
22. Braun, M.; Kellner, L. Comparison of Machine Learning and Stress Concentration Factors-based Fatigue Failure Prediction in Small-scale Butt-welded Joints. *Fatigue Fract. Eng. Mater. Struct.* **2022**, *45*, 3403–3417. [CrossRef]
23. Zhan, Z.; Li, H. Machine Learning Based Fatigue Life Prediction with Effects of Additive Manufacturing Process Parameters for Printed SS 316L. *Int. J. Fatigue* **2021**, *142*, 105941. [CrossRef]
24. Shi, T.; Sun, J.; Li, J.; Qian, G.; Hong, Y. Machine Learning Based Very-High-Cycle Fatigue Life Prediction of AlSi10Mg Alloy Fabricated by Selective Laser Melting. *Int. J. Fatigue* **2023**, *171*, 107585. [CrossRef]
25. Konda, N.; Verma, R.; Jayaganthan, R. Machine Learning Based Predictions of Fatigue Crack Growth Rate of Additively Manufactured Ti6Al4V. *Metals* **2022**, *12*, 50. [CrossRef]
26. Jat, V.K.; Patil, R.U.; Samant, S.S. Influence of Scanning Strategies on the Tensile and Fatigue Properties of Direct Metal Laser Sintering-Printed Co-Cr-Mo Alloy. *J. Mater. Eng. Perform.* **2025**, *34*, 7479–7495. [CrossRef]
27. Jat, V.K.; Patil, R.U.; Yadav, V.K. Fracture Toughness and Fatigue Crack Growth in DMLS Co-Cr-Mo Alloy: Unraveling the Role of Scanning Strategies. *Theor. Appl. Fract. Mech.* **2024**, *134*, 104681.
28. Bera, A.K.; Bilias, Y. The MM, ME, ML, EL, EF and GMM Approaches to Estimation: A Synthesis. *J. Econom.* **2002**, *107*, 51–86. [CrossRef]
29. Shen, L.; Qian, Q. A Virtual Sample Generation Algorithm Supporting Machine Learning with a Small-Sample Dataset: A Case Study for Rubber Materials. *Comput. Mater. Sci.* **2022**, *211*, 111475. [CrossRef]
30. Huang, Q.; Hu, D.; Wang, R.; Sergeichev, I.; Sun, J.; Qian, G. Fatigue Short Crack Growth Prediction of Additively Manufactured Alloy Based on Ensemble Learning. *Fatigue Fract. Eng. Mater. Struct.* **2025**, *48*, 1847–1865. [CrossRef]

31. Zhang, X.C.; Gong, J.G.; Xuan, F.Z. A Physics-Informed Neural Network for Creep-Fatigue Life Prediction of Components at Elevated Temperatures. *Eng. Fract. Mech.* **2021**, *258*, 108130. [CrossRef]
32. Nadda, M.; Shah, S.K.; Roy, S.; Yadav, A. CFD-Based Deep Neural Networks (DNN) Model for Predicting the Hydrodynamics of Fluidized Beds. *Digit. Chem. Eng.* **2023**, *8*, 100113. [CrossRef]
33. Kim, D.; Kim, J.; Kim, J. Elastic Exponential Linear Units for Convolutional Neural Networks. *Neurocomputing* **2020**, *406*, 253–266. [CrossRef]
34. Wang, H.; Li, B.; Gong, J.; Xuan, F.-Z. Machine Learning-Based Fatigue Life Prediction of Metal Materials: Perspectives of Physics-Informed and Data-Driven Hybrid Methods. *Eng. Fract. Mech.* **2023**, *284*, 109242. [CrossRef]
35. Lei, L.; Li, B.; Wang, H.; Huang, G.; Xuan, F. High-Temperature High-Cycle Fatigue Performance and Machine Learning-Based Fatigue Life Prediction of Additively Manufactured Hastelloy X. *Int. J. Fatigue* **2024**, *178*, 108012. [CrossRef]

https://doi.org/10.3390/met16030249